Solar Energy 300 (2025) 113859

Contents lists available at ScienceDirect

Solar Energy

journal homepage: www.elsevier.com/locate/solener

Photothermal polyurethane coatings with functionalized nanoparticles and quasi-liquid layer for enhanced anti-icing and solar-assisted de-icing

Mohammad Bakhtiari [a,*], Gelareh Momen [a,b], Reza Jafari [a]

[a] Department of Applied Sciences, University of Quebec in Chicoutimi (UQAC), 555, boul. de l'Université, Chicoutimi, Quebec G7H 2B1, Canada
[b] Department of Aerospace Engineering, École de Technologie Supérieure (ETS), Montréal, Quebec H3C 1K3, Canada

ARTICLE INFO

Keywords:
Polyurethane coatings
Ice adhesion strength
Photothermal
De-icing
Magnetic Fe_3O_4
Quasi −liquid layer

ABSTRACT

Polyurethane (PU) coatings effectively mitigate ice accumulation on surfaces in low-temperature conditions. Unlike traditional de-icing methods that can be ineffective, costly, or environmentally harmful, PU photothermal coatings offer environmental and economic benefits. They not only improve anti-icing properties and de-icing efficiency but also address critical operational and sustainability challenges associated with harsh winter environments.

This study aims to develop a simple yet effective strategy for producing PU coatings with enhanced anti-icing and de-icing performance by methodically incorporating various forms of iron oxide nanoparticles—including Fe_3O_4 (FPU), silicone oil–coated Fe_3O_4 (SiFPU), and hydroxyl (OH)-functionalized Fe_3O_4 (FOHPU)—at concentrations from 0.5 % to 10 % to investigate their influence on mechanical, photothermal, and icephobic behavior.

PU coatings were fabricated and subjected to characterization using SEM, FTIR, UV–Vis spectroscopy, and tensile testing. IR thermography was used to evaluate photothermal performance under 1 sun xenon illumination. Icephobic properties was evaluated through push-off tests in a cold room under both with and without simulated sunlight. Photothermal de-icing was assessed using simulated sunlight and push-off tests (ice adhesion strength) in a cold room, both with and without simulated sunlight. The endurance of the coatings through repeated icing/de-icing cycles was assessed.

UV–Vis spectroscopy revealed improved light absorption, with the band gap of Fe_3O_4 nanoparticles being reduced by the silicone oil coating and hydroxyl functionalization (by 2.3 and 2.55 eV, respectively). The results indicate that the icephobic performance of PU coatings is considerably improved by using surface-functionalized nanoparticles. Also, 10FOHPU demonstrated a marked enhancement in mechanical properties, with a Young's modulus of 140 ± 6.2 MPa and a tensile strength of 6.3 ± 0.2 MPa (compared to 106.1 ± 4.1 MPa and 6.1 ± 0.4 MPa for unmodified PU). In addition, the presence of a quasi-liquid layer on the FOHPU coatings was verified by ATR-FTIR spectroscopy conducted at sub-zero temperatures. Notably, 10SiFPU exhibited the lowest ice adhesion (40 ± 8 kPa) after 20 min of light exposure. These results highlight the potential of SiFPU and FOHPU coatings for sustainable and efficient anti-/de-icing applications. This optimized performance is facilitated by tailored nanoparticle surface chemistry.

1. Introduction

Ice accumulation on outdoor equipment disrupts industrial production and daily life [1,2]. It can cause mechanical failures, reduced efficiency, and safety hazards in critical energy infrastructure, such as wind turbines and power lines, as well as in transportation systems, including aircraft and presents a major challenge for solar energy systems as well [3–8]. Researchers are developing icephobic and anti-icing surfaces and studying ice formation to better manage the buildup of ice [5,9,10]. The management ice buildup can be categorized as either de-icing or anti-icing approaches. Anti-icing techniques prevent ice formation, whereas de-icing techniques remove accumulated ice [11]. Icephobic materials can reduce ice adhesion strength, decrease ice accretion rates, and delay freezing time or temperature [12]. In extreme weather, icephobic materials may be less effective, so it is crucial to develop de-icing and anti-icing materials [13,14]. De-icing technologies, which use

* Corresponding author.
E-mail address: mbakhtiari@etu.uqac.ca (M. Bakhtiari).

https://doi.org/10.1016/j.solener.2025.113859
Received 25 June 2025; Received in revised form 25 July 2025; Accepted 3 August 2025
Available online 9 August 2025

mechanical, thermal, chemical, and ultrasonic guided wave techniques, eliminate ice accumulation instead of preventing it [15]. However, these techniques often suffer from high energy consumption, low efficacy, damage to the infrastructure requiring protection, and significant pollution [16,17]. Among them, thermal de-icing approaches remove ice by applying controlled heat, efficiently melting and dislodging ice from surfaces in targeted settings like aircraft, wind turbines, and photovoltaic panels. Compared to chemical agents, these systems minimize environmental harm and reduce the likelihood of surface damage commonly associated with mechanical methods. Nevertheless, their practical use requires a steady energy supply and often involves higher upfront installation expenses.[18].

Photothermal materials are gaining popularity because of their sustainable and energy-efficient approach to ice accumulation. They convert light energy into heat, melting ice directly on surfaces via solar energy or other light sources rather than external power sources [17–25]. Photothermal materials, particularly transition metal oxides like iron oxide (Fe_3O_4), have shown promise in this area due to their capacity to absorb light and convert it into heat. Semiconductors, composed of transition metal oxides This process involves electronic excitation, where photons promote electrons from the valence band to the conduction band, resulting in energy dissipation as thermal radiation. The efficacy of this conversion relies on nanoparticle surface modifications and their optical bandgap [26,27].

Recently, researchers have developed icephobic surfaces using various photothermal materials including black oxides, plasmonic nanoparticles, cermets, and carbon compounds [28–31]. These surfaces are categorized according to their solar-energy usage and surface-modification capabilities. The first group integrates micro/nanostructures (SiC/CNTs–TiN-PTFE films) to achieve superhydrophobic [31] or lubricant-infused surfaces [28], but they only partially use broad-spectrum solar radiation, particularly in the near-infrared (NIR). Therefore, they offer insufficient photothermal effects. The second category harnesses nearly the entire solar spectrum through cermets [22] or carbon-based materials [32], but these coatings fail to remove melted water promptly because of a lack of superhydrophobicity or self-lubricating properties, which reduces photothermal efficiency and increases the risk of ice reformation [33]. In a recent paper, however, Wu et al. [34] grafted polydimethylsiloxane (PDMS) brushes onto a candle soot–based structure, combining superhydrophobicity with efficient sunlight trapping to produce a self-cleaning surface. However, an often-overlooked factor in solar anti-/de-icing systems is the spectral characteristic of heat radiation, particularly spectral selectivity. Heat loss through thermal re-radiation from the absorber to the environment greatly affects the overall efficacy of solar absorbers. Although blackbody absorbers exhibit near-perfect absorption/emission across the UV–visible–infrared (IR) spectrum (0.3–20 mm), their high IR emissivity diminishes their solar–thermal conversion efficacy [33]. Yang et al. develop a superhydrophobic photothermal coating using acrylic resin, diatomaceous earth, and encapsulated Fe_3O_4 nanoparticles, tested under simulated sunlight irradiation at 1 kW/m^2. However, their investigation overlooks the functionalization of these particles for optimal photothermal performance and challenges with larger ice formations [35].

Previous studies have primarily focused on either superhydrophobic surfaces or photothermal coatings that utilize only a portion of the solar spectrum. In contrast, this study investigates the performance of functionalized Fe_3O_4 nanoparticles embedded in polyurethane matrices under simulated full-spectrum sunlight using a xenon light source. Polyurethane was selected for its mechanical properties and strong surface adhesion, making it an ideal matrix for photothermal applications. The innovative approach employed in this research involves the incorporation of three types of Fe_3O_4 nanoparticles (bare, hydroxyl-functionalized, and silicone oil–coated) and their influence on the surface properties of the coatings and their photothermal performance. Notably, the incorporation of hydroxyl-functionalized nanoparticles promotes the formation of a quasi-liquid layer within the polymer matrix, which contributes to reduced ice adhesion without the need for external heating. The overarching goal is to optimize the synergy between passive (surface coating) and active (photothermal) anti-/de-icing mechanisms. By evaluating nanoparticle dispersion, photothermal response, and mechanical integrity, this research aims to advance the development of multifunctional, durable coatings for effective and energy-efficient anti-/de-icing in real-world applications.

2. Materials and experimental setup

2.1. Materials

Three types of iron oxide (Fe_3O_4) nanoparticles were used to formulate the polyurethane coatings: OH-functionalized dry powder Fe_3O_4, silicone oil–coated Fe_3O_4, and bare dry powder Fe_3O_4, all sourced from Us Nano at 99 % purity. The nanoparticles had an average size of 20–30 nm and a specific surface area of 40–60 m^2/g. SETALUX® 1909 BA, an acrylic polyol with 5 wt% hydroxyl content and 75 % solid content, was provided by Alnex Chemical Company as the base resin. Tolonate™ HDB 75B, with an NCO content of 16.5 % ± 0.3 %, served as the hardener and was supplied by Vencorex. N-Butyl acetate (99 %) from Thermo Fisher Scientific was used as the solvent to adjust the viscosity of the coating mixture. The substrates for the coating application were aluminum sheets (A6061), which were cleaned with distilled water followed by three rounds of acetone for thorough surface preparation.

2.2. Coating preparation

Polyurethane coatings were prepared by mixing polyols, Fe_3O_4 nanoparticles, and a solvent. Ultrasonication at 100 Hz for 20 min dispersed the nanoparticles uniformly in the mixture. After homogeneous dispersion was achieved, a hardener was added. A reference mixture without nanoparticles was prepared for comparison. The coating mixtures were then applied to pretreated substrates using a spin coater. The coated samples were placed in a clean room at room temperature for one week to allow the coatings to fully cure. The dry thickness of the coatings, measured using a micrometer, was approximately 150 ± 10 μm.

To differentiate the formulations, the samples were labeled based on the type of nanoparticles and their coating content. The first part of the label indicates the nanoparticle concentration, whereas the second part identifies the nanoparticle type, with PU as the matrix (Table 1). For example, “FPU” signified coatings with bare Fe_3O_4 nanoparticles, “SiFPU” referred to silicone oil–coated Fe_3O_4 nanoparticles, and “FOHPU” indicated hydroxyl-functionalized Fe_3O_4 nanoparticles. This labeling scheme enabled the clear identification of the study’s specific variables.

Table 1
Composition of the PU coatings containing iron oxide (Fe_3O_4) nanoparticles (Each sample contained 100 g of polyol, 56.1 g of hardener, and 24 g of solvent).

Sample	Fe_3O_4 (g)	Silicone oil–coated Fe_3O_4 (g)	OH-functionalized Fe_3O_4 (g)
PU	0	0	0
0.5FPU	0.58	0	0
1FPU	1.18	0	0
5FPU	6.16	0	0
10FPU	13.00	0	0
0.5SiFPU	0	0.58	0
1SiFPU	0	1.18	0
5SiFPU	0	6.16	0
10SiFPU	0	13.00	0
0.5FOHPU	0	0	0.58
1FOHPU	0	0	1.18
5FOHPU	0	0	6.16
10FOHPU	0	0	13.00

2.3. Characterization

Fourier transform infrared (FTIR) spectra of the polyurethane coatings containing Fe_3O_4 nanoparticles were obtained using a FTIR spectrometer (PerkinElmer, Spectrum Two, USA) in attenuated total reflection (ATR) mode, covering the infrared wavelength range of 400–4000 cm^{-1}. Scanning electron microscopy was performed to examine the coatings' morphology (JEOL JSM-6480LV, JEOL USA Inc., Peabody, MA, USA). . Before imaging, the samples were sputter-coated with a thin platinum layer to enhance surface conductivity.

Ultraviolet–visible (UV–Vis) spectroscopy was performed to investigate the optical absorption properties of the Fe_3O_4 nanoparticles. The analysis involved Fe_3O_4 nanoparticles dispersed in water, silicone oil–-coated Fe_3O_4 nanoparticles, and hydroxyl-functionalized Fe_3O_4 nanoparticles. Absorption spectra were recorded for each sample and generated Tauc plots to estimate the optical bandgaps. These measurements provided insights into the light absorption capabilities of the nanoparticles, which are critical for evaluating their potential photothermal performance.

Tensile properties were evaluated at room temperature using a TA. XTPlus 100 testing machine (TA.TX Plus100C, Stable Micro System, Godalming, UK) equipped with a 100 kg load cell. Rectangular film strips measuring 10 × 1.25 cm were prepared for each sample. The thickness of each strip was determined using a micrometer accurate to 0.01 mm. For each formulation, at least five replicate samples were prepared and subjected to analysis. The ASTM D 2370 standard testing method was used to determine the tensile behavior of freestanding films. Each formulation was tested with five samples at a constant crosshead speed of 5 mm/min at an ambient temperature of 24 ± 1 °C.

2.3.1. Surface roughness

Surface roughness was evaluated using a Profilm3D Filmetrics® optical profilometer equipped with white light interferometry (WLI). This approach provides precise surface profiling and roughness measurements, with a resolution of up to 50 nm. For smooth surfaces, the phase-shifting interferometry (PSI) mode was used with an accuracy of 1 nm on the Angstrom scale. The measurements covered an area of 400 × 400 μm, with six randomly selected regions analyzed per sample to ensure reliability.

2.3.2. Wettability analysis

The relationship between the water contact angle (WCA) and ice adhesion strength reveals the complex atomic interactions that influence the interaction of water droplets with surfaces. The wettability characteristics of the coatings were examined to assess the effects of the different Fe_3O_4 nanoparticles. WCA measurements were performed using the sessile drop method on a Krüss™ DSA100 goniometer at a controlled room temperature of 25 ± 0.5 °C. A 4 μL droplet of distilled water was placed on the sample surface, and the measurement was recorded using ADVANCE drop shape analysis software. The sliding angle (SA) was also evaluated using the same instrument equipped with a tilting stage. A 35 μL water droplet was deposited on the sample, which was tilted at 60°/min until the droplet began to slide or roll off up to a maximum angle of 60°. Contact angle hysteresis (CAH) were calculated as the difference between the advancing and receding contact angles. The SA was recorded 0.5 s before droplet motion began. Both the WCA and SA values were calculated using tangent approximation methods, with the fitting model mathematically representing the curvature of the droplet.

2.3.3. Photothermal properties

To evaluate the photothermal properties of the fabricated samples, the coatings were exposed to a xenon lamp emitting approximately 1 kW/m^2 (Fig. 1a). Fig. 1b presents the spectral power distribution of the SLS401 light source. The experiment was conducted at room temperature to simulate typical environmental conditions. This light intensity mimics sunlight exposure, allowing investigation of the coatings' ability to absorb and convert sunlight into heat. The samples were placed under the lamp, and their temperature increase over time was measured using an infrared camera to assess the photothermal efficiency of the coatings at increasing temperatures relative to the ambient environment. Temperature increase reflects the coatings' effectiveness in converting light energy into thermal energy.

2.3.4. Thermography

A thermal camera (Optris Pi450i, Optris, Berlin, Germany) and its software (Optris PIX Connect Rel.1.2.1030.0) provided a detailed view of surface temperature. The camera, equipped with a 382 × 288 pixel uncooled microbolometer and an 18° × 14° field of view (FOV), was positioned about 40 cm from the sample and powered on for at least 30 min before measurements to ensure thermal equilibrium. The camera's noise equivalent temperature difference (NETD) was 60 mK.

2.4. Icephobic properties

2.4.1. Temperature-controlled ATR-FTIR for surface freezing behavior

ATR-FTIR spectroscopy (Perkin Elmer Spectrum II) was used to investigate the coating–water interface at low temperatures and the presence of a quasi-liquid layer (QLL). A custom cold-base setup ensured precise temperature control (±0.5 °C) at the coating–prism interface. To

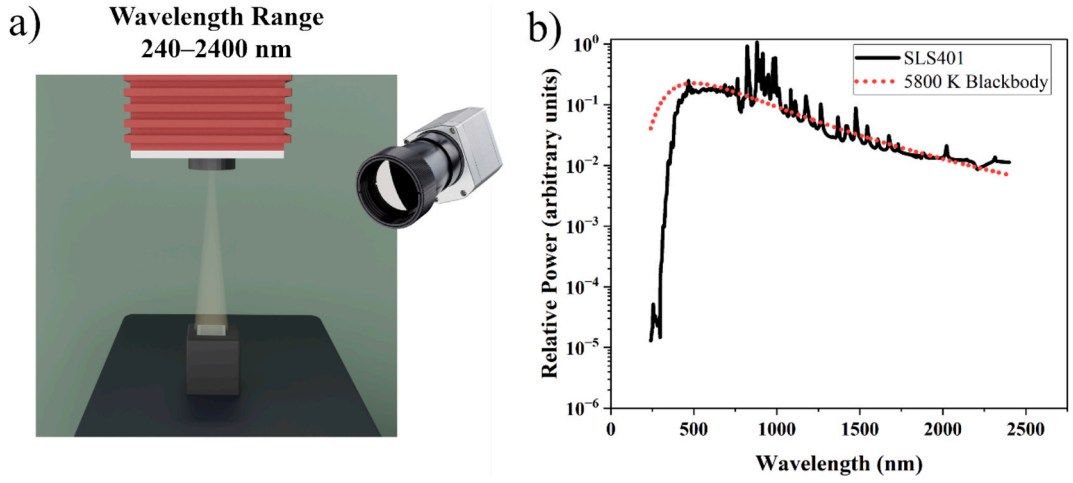

Fig. 1. a) Schematic illustrating the xenon light projected onto the surface; b) spectral power distribution of the sls401 light. Source. The spectrum is displayed on a logarithmic scale to clearly show both the overall shape and the spectral lines

avoid interference between the absorption bands of the amine groups in the coatings and the hydroxyl groups of water, D_2O was used instead of H_2O, as their freezing behaviors are nearly identical. The coating samples were soaked in D_2O before collecting continuous FTIR spectra during a temperature ramp up from + 25 to −20 °C at a cooling rate of 0.5 °C/min. This approach, using ATR-FTIR spectroscopy with D_2O to study ice formation and QLL, builds on similar methodologies established in our group's previous work, as demonstrated in Koochaki et al. [36].

2.4.2. Photothermal de-icing under simulated sunlight

The experimental setup for measuring photothermal de-icing performance involved a xenon light source (SLS 401)–simulated solar radiation, directing a collimated light beam onto the surfaces (Fig. 2a). The illumination spot had a diameter of 3.5 ± 0.2 mm with a maintained power density P of ± 0.01 suns ($kW{\cdot}m^{-2}$). A mechanical shutter controlled the illumination intermittently. A 100 μL droplet of distilled water was placed on the coated surface and frozen at –10 °C to create an ice droplet for evaluating the de-icing capacity of the coatings. After freezing, the sample was exposed to simulated sunlight under controlled conditions. A high-speed camera recorded the de-icing process to monitor ice behavior in real time. Two main parameters were defined for this study: (i) starting de-icing time, representing the time from the beginning of illumination to the first visible movement or melting at the ice–surface interface; and (ii) complete de-icing time, indicating the total time required for full melting of the ice droplet. An infrared (IR) camera was used to simultaneously monitor the surface temperature.

2.4.3. Ice adhesion strength

The ice adhesion strength of the samples was determined using a push-off test. In this test, an ice cylinder was produced over 18 h by placing a 1.5 cm diameter cylindrical plastic mold on the surface and filling it with deionized water in a cold chamber at –10 °C. A digital force gauge (FG-3005, Shimpo Instruments, Lynbrook, NY, USA) measured the force required to detach the ice cylinders from the coating surface. The force gauge tracked the shear force via a remote computer-operated interface until the ice broke from the surface. The force meter probe applied force until the frozen cylinder detached from the sample surface. To ensure consistent and repeatable shear loading, the distance between the digital force gauge and the coating surface was fixed at 1 mm throughout all tests, minimizing variability in the applied force direction and contact geometry. Each formulation was tested with three replicate samples, and the results are presented with corresponding standard deviations. The adhesion stress was calculated by dividing the maximum force by the area under the ice. Furthermore, the same process was repeated 14 times to assess the durability of the coatings under repeated icing/de-icing cycles.

2.4.4. Ice adhesion strength under simulated sunlight

A push-off test under simulated sunlight evaluated how photothermal heating affects ice adhesion strength (Fig. 2b). After 24 h of freezing at −10 °C, the cylindrical molds filled with deionized water remained stable on the coated surfaces in a cold environment. The xenon light source was then activated for 20 min to induce surface heating, as detailed in Section 2.3.3. The ice adhesion strength was measured using the procedure described in Section 2.4.3, allowing for a direct comparison between illuminated and non-illuminated conditions.

3. Results and discussion

3.1. Surface morphology and chemical composition

3.1.1. ATR-FTIR spectroscopy

The FTIR spectra of Fe_3O_4, hydroxyl-functionalized Fe_3O_4, and silicone oil–coated Fe_3O_4 nanoparticles for all samples (Fig. 3) show characteristic absorption bands linked to magnetite, confirming the persistence of the core Fe_3O_4 structure after surface alteration. A strong absorption band near 550 cm^{-1} corresponds to the Fe–O stretching vibration, whereas a band at 1628 cm^{-1} is attributed to Fe–O bending modes [37]. The distinct absorption band at 622 cm^{-1} corresponds to the ν_1 vibrational mode of the Fe–O bond, representing a characteristic infrared feature of Fe_3O_4 nanoparticles [38]. The hydroxyl-functionalized Fe_3O_4 (Fe_3O_4-OH) spectrum shows a broad band at 3418 cm^{-1}, attributed to O–H stretching vibrations, and confirms the presence of hydroxyl groups on the nanoparticle surface [37]. In contrast, the silicone oil–coated Fe_3O_4 nanoparticles exhibit new peaks, notably at 2984 and 2889 cm^{-1}, corresponding to C–H stretching vibrations, as well as at 1263, 1092, and 1021 cm^{-1}, which are attributed to Si–O–Si and Si–CH_3 stretching vibrations. Additional peaks at 800 and 622 cm^{-1} are associated with Si–C and Si–O vibrations, respectively, confirming the presence of a silicone-based coating [39–41]. These distinct peaks in Fe_3O_4-OH and the silicone oil–coated Fe_3O_4 samples indicate the presence of these groups on the surface of the nanoparticles.

3.1.2. SEM analysis

The analysis of the surface characteristics of three coatings—10FPU,

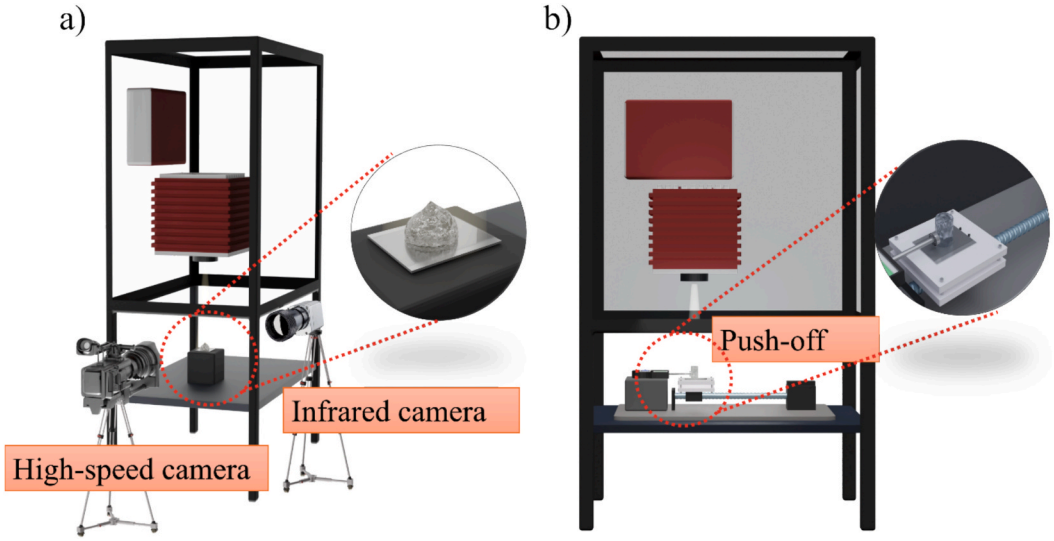

Fig. 2. Experimental setup of a) photothermal de-icing tests under simulated sunlight; b) ice adhesion strength testing under simulated sunlight.

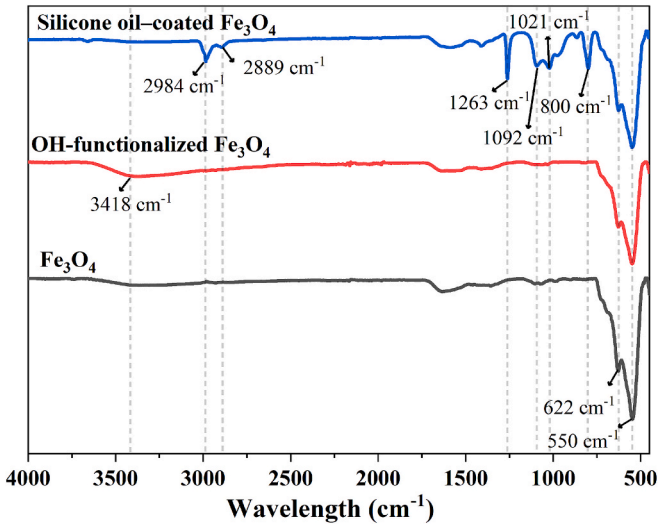

Fig. 3. ATR-FTIR spectra of Fe_3O_4 (*black line*), Fe_3O_4-OH (*red line*), and silicone oil–coated Fe_3O_4 (*blue line*) nanoparticles. (For interpretation of the references to colour in this figure legend, the reader is referred to the web version of this article.)

10FOHPU, and 10SiFPU—revealed notable differences in nanoparticle distribution and surface morphology (Fig. 4). The Fe_3O_4 nanoparticles in these coatings were observed to have an average size of 20–30 nm. The 10FPU coating, which contains Fe_3O_4 nanoparticles, showed a uniform particle distribution; however, the absence of functional groups limits interaction with the polyurethane (PU) binder, resulting in a less cohesive surface. In contrast, the 10FOHPU coating, which contains hydroxyl-functionalized Fe_3O_4 nanoparticles, demonstrated improved adhesion and distribution. The hydroxyl groups enhance the compatibility with the PU matrix, leading to a more even dispersion and smoother surface finish [42,43]. This functionalization improves interaction with the binder, reducing agglomeration and enhancing the coating's mechanical properties. The 10SiFPU coating features silicone oil–coated Fe_3O_4 nanoparticles, which significantly alter surface tension dynamics and promote greater nanoparticle migration to the surface during curing. This occurs because of the differing polarities between the silicone oil and PU binder, which reduces the compatibility. Consequently, the 10SiFPU coating exhibits a higher density of surface particles than the other two coatings, enhancing the surface properties and potentially improving the durability and resistance to environmental factors.

3.1.3. Wettability behavior

The wettability behavior of the coatings was evaluated through WCA, contact angle hysteresis (CAH), and SA measurements; such measurements are essential for understanding water molecule interactions with the surface (Fig. 5). The polyurethane (PU) coating without nanoparticles showed a WCA of 89°, a CAH of 36°, and a SA of 25°. As the concentration of Fe_3O_4 nanoparticles (FPU) increased, both the CAH and SA values increased, likely because of the greater surface roughness of the coating. This roughness leads to greater hysteresis, making it more difficult for water droplets to slide off the surface. A high CAH indicates a strong pinning of water droplets, which delays removal and enhances ice adhesion strength, thus reducing the coating's anti-icing effectiveness. In the case of silicone oil–coated Fe_3O_4 nanoparticles (SiFPU), higher nanoparticle concentrations decreased both CAH and SA values, indicating improved droplet mobility and reduced water adhesion. Silicone oil lowers the surface tension, facilitating the migration of nanoparticles to the surface and increasing WCA. The SA reduction was more pronounced at higher concentrations of silicone oil–coated nanoparticles, enhancing the anti-icing properties of the coating. For hydroxyl-functionalized Fe_3O_4 (FOHPU) coatings, increasing the nanoparticle concentration led to a slight decrease in WCA, accompanied by an increase in CAH and SA. However, this increase was not as marked as that for the FPU coatings, suggesting that hydroxyl groups only slightly improve the surface wettability without greatly increasing the surface roughness or hysteresis. This increase in hysteresis is attributed to the enhanced surface hydrophilicity at higher FOHPU concentrations, which results in a lower receding contact angle, as shown in Fig. 5b [44].

3.1.4. Surface roughness

Surface roughness was measured using profilometry, with the "S_q" parameter quantifying the increase in roughness (Fig. 6). The PU coating had a roughness of 28 nm. For the FPU coatings, the roughness increased from 40 nm at 0.5FPU to 130 nm at 10FPU, indicating a marked increase with higher nanoparticle concentration. SiFPU coatings exhibited even greater roughness, increasing from 35 nm at 0.5SiFPU to 170 nm at 10SiFPU, suggesting that silicone oil–coated nanoparticles enhance surface roughness. In contrast, FOHPU coatings showed moderate increases, with roughness ranging from 35 nm at 0.5FOHPU to 101 nm at 10FOHPU (Fig. 7). This trend reflects the effects of nanoparticle concentration and surface chemistry on roughness. The silicone oil–coated nanoparticles (SiFPU) had the highest surface roughness because of the surface tension of the silicone oil, which promotes the migration of nanoparticles to the coating surface during curing. This accumulation at the surface creates a more pronounced roughness than that of the other coatings. FPU coatings exhibited a steady increase in roughness with nanoparticle concentration, whereas the FOHPU coatings exhibited a gradual increase in roughness because of the compatibility of hydroxyl groups with the polyurethane matrix, resulting in less pronounced surface roughening. These findings highlight the influence of nanoparticle type and concentration on surface roughness, with silicone oil–coated nanoparticles producing the greatest roughness.

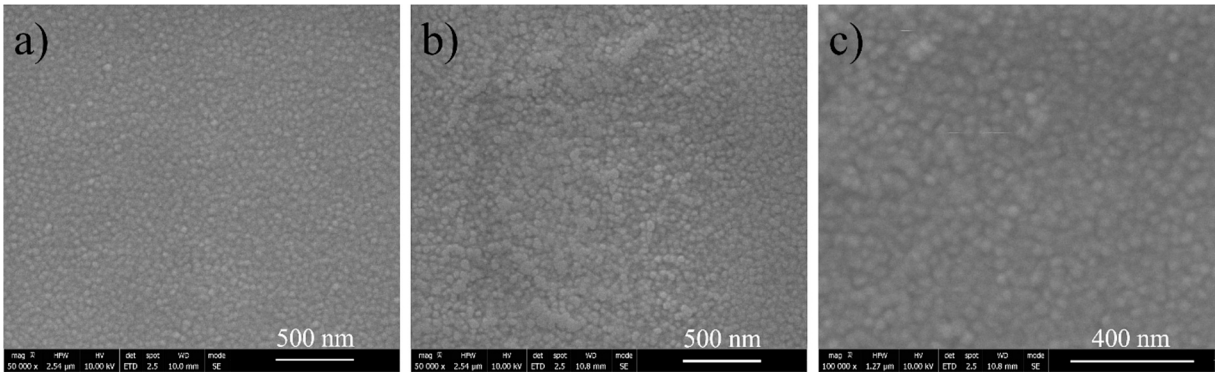

Fig. 4. SEM images of a) 10FPU, b) 10FOHPU, and c) 10SiFPU surfaces.

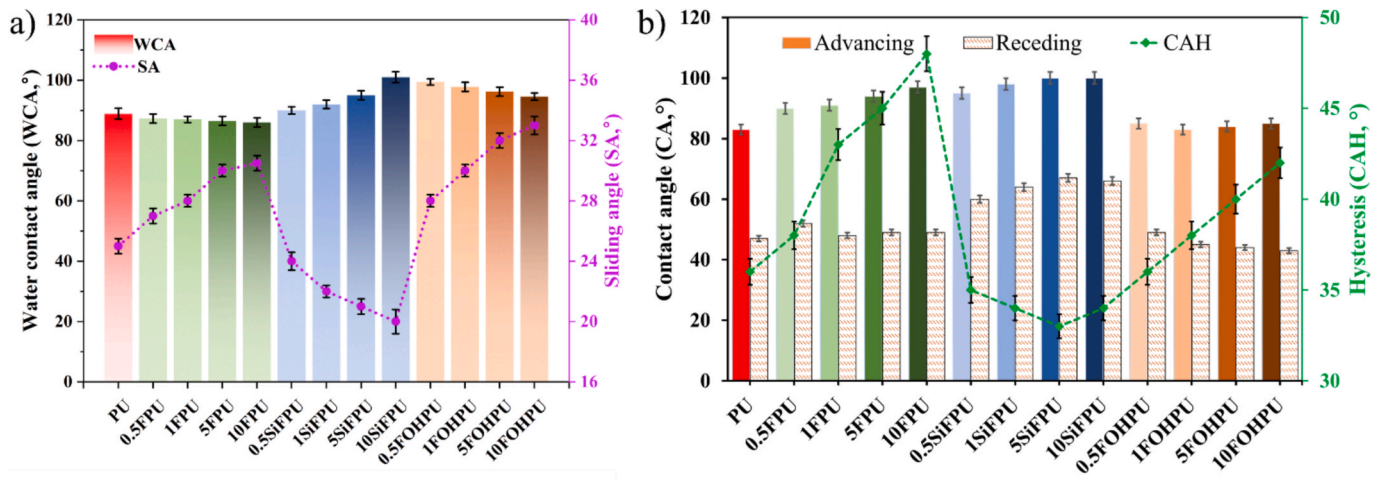

Fig. 5. Wetting properties of the PU coatings differing in iron oxide (Fe_3O_4) nanoparticles and concentrations for the various FPU, SiFPU, and FOHPU coatings; (a) water contact angle and sliding angles; (b) contact angle hysteresis and advancing and receding.

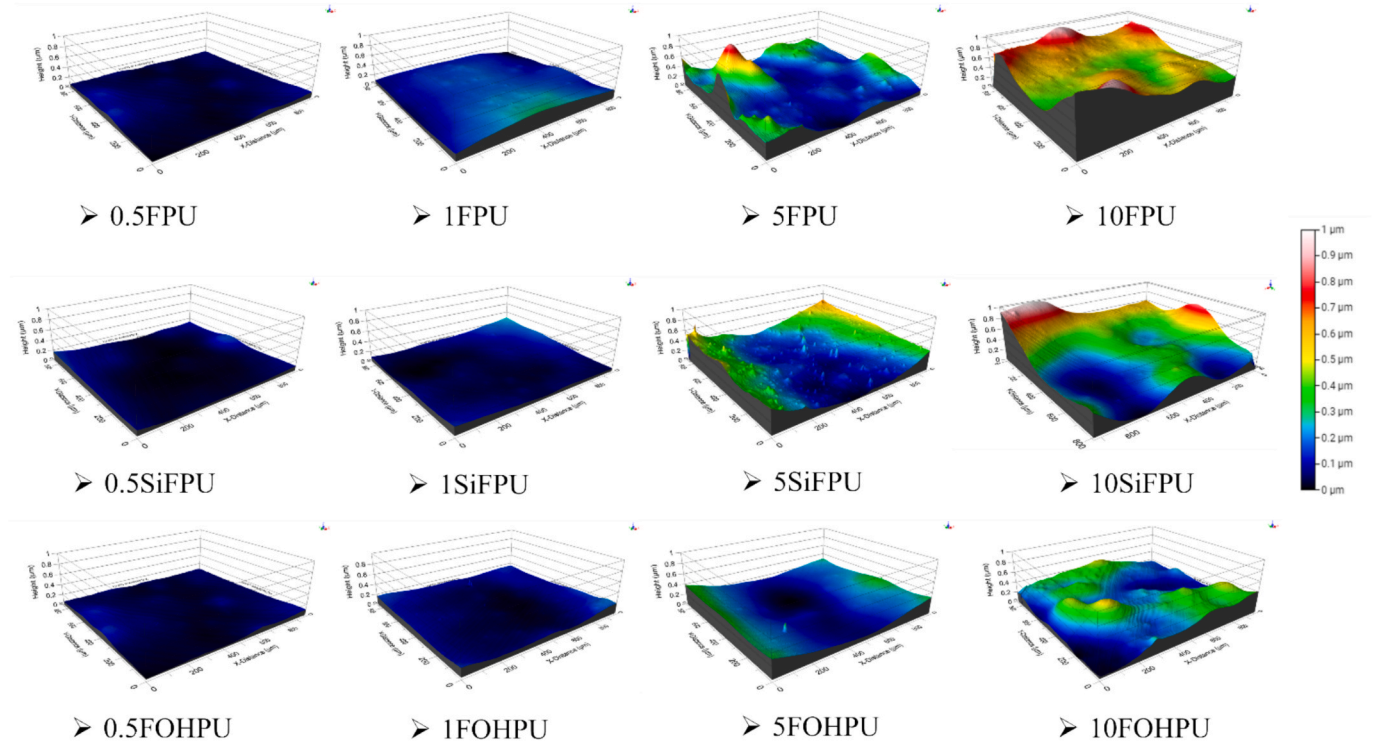

Fig. 6. Three-dimensional (3D) roughness profiles of the prepared PU coatings varying in their iron oxide (Fe_3O_4) nanoparticle concentrations and composition.

3.2. Mechanical properties

Tensile tests were performed to assess the mechanical properties of PU and three modified PU coatings (10FPU, 10SiFPU, and 10FOHPU). The elongation at break, Young's modulus, and tensile strength of the coatings are summarized in Table 2. Stress–strain curves (Fig. 8) provide data on the response of materials to tensile loading. The baseline PU coating had a tensile strength of 6.1 ± 0.4 MPa, elongation at break of 64 %, and a Young's modulus of 106.1 ± 4.1 MPa. Adding unaltered Fe_3O_4 (10FPU) greatly reduced tensile strength and elongation at break relative to pure PU, decreasing to 4.2 ± 0.3 MPa and 30.8 ± 5.4 %, respectively, for 10FPU. Therefore, the unmodified Fe_3O_4 particles act as stress concentrators within the PU matrix, leading to premature failure. Among the samples, silicone oil–coated Fe_3O_4 (10SiFPU) exhibited the weakest mechanical properties. Although its elongation at break (42.7 % ± 1.5 %) surpassed that of 10FPU (30.0 %), both its tensile strength (3.7 ± 0.2 MPa) and Young's modulus (53 ± 2.7 MPa) were significantly lower than those of 10FPU. Its Young's modulus was about 50 % lower and tensile strength 38.3 % lower than that of pure PU, likely because the silicone oil layer hindered strong interfacial bonding [45].

In contrast, the 10FOHPU composite, having hydroxyl-functionalized Fe_3O_4, showed the best mechanical properties. It achieved a slightly higher tensile strength (6.3 ± 0.2 MPa) than pure PU, a 5 % increase, yet a marked 32 % increase in Young's modulus (140 ± 6.2 MPa), representing a substantial increase relative to pure PU. The elongation at break for 10FOHPU was 49.4 % ± 5.1 %, which was much lower than that of pure PU but higher than that of 10FPU and 10SiFPU. The hydroxyl groups on the Fe_3O_4 surface enhance the performance of 10FOHPU by promoting strong hydrogen bonding with the urethane

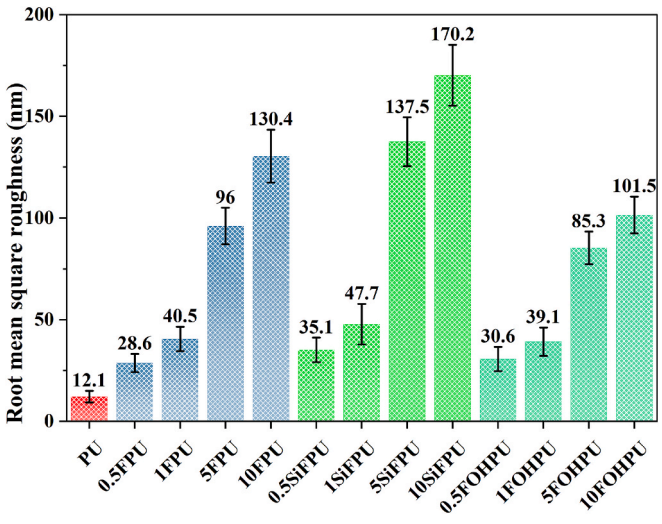

Fig. 7. Surface roughness (S_q) of PU coatings with different iron oxide (Fe_3O_4) nanoparticle concentrations and compositions.

Table 2
Tensile isotherms of the PU, 10FPU, 10SiFPU, and 10FOHPU coatings.

Sample	Tensile strength at break (MPa)	Elongation at break (%)	Young modulus (MPa)
PU	6.1 ± 0.4	64.6 ± 4.3	106.1 ± 4.1
10FPU	4.2 ± 0.3	30.8 ± 5.4	81.2 ± 5.6
10SiFPU	3.7 ± 0.2	42.7 ± 1.5	53 ± 2.7
10FOHPU	6.3 ± 0.2	49.4 ± 5.1	140 ± 6.2

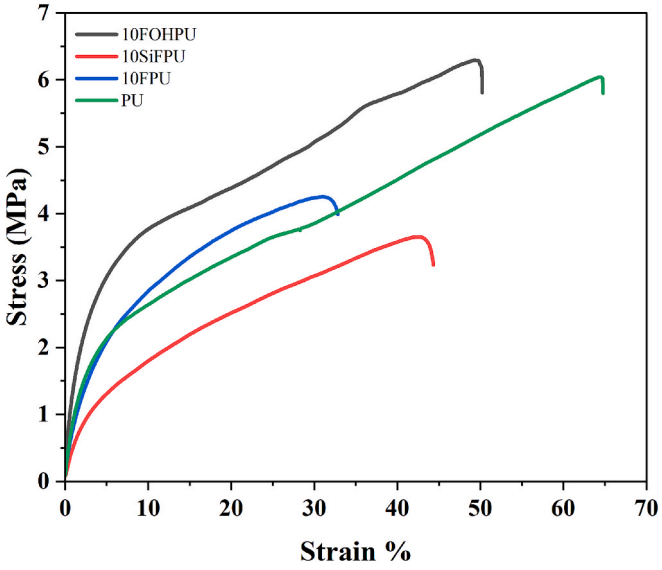

Fig. 8. Stress–strain curves of the PU, 10FPU, 10SiFPU, and 10FOHPU coatings.

groups in the PU matrix and therefore improving interfacial adhesion. This interaction contributes to a stiffer and stronger material, as evidenced by the increased Young's modulus and tensile strength. The hydroxyl-functionalized Fe_3O_4 acts as a cross-linking agent [46,47].

3.3. Ultraviolet–visible (UV–Vis) spectroscopy

UV–Vis spectroscopy revealed notable differences in the optical bandgaps of the various Fe_3O_4 nanoparticle samples. The Fe_3O_4 nanoparticles dispersed in water had a bandgap of 2.6 eV (Fig. 9a). The silicone oil–coated Fe_3O_4 nanoparticles had a lower bandgap (2.29 eV (Fig. 9c), whereas the hydroxyl-functionalized Fe_3O_4 nanoparticles had a bandgap of 2.55 eV (Fig. 9b). The lower band gaps of the coated and functionalized nanoparticles indicate improved light absorption relative to uncoated nanoparticles. This enhanced absorption is expected to increase the photothermal efficiency of the coatings, emphasizing the role of surface modification in optimizing the nanoparticles for photothermal applications [48].

3.4. Photothermal properties

The photothermal properties of the coatings were assessed by measuring the temperature change (ΔT) after irradiation for 20 min. The PU coating on an aluminum surface increased 11 °C after 20 min (Fig. 10). For all nanoparticle types—bare Fe_3O_4 (FPU), silicone oil–-coated Fe_3O_4 (SiFPU), and hydroxyl-functionalized Fe_3O_4 (FOHPU)—the temperature increase (ΔT) correlated positively with nanoparticle concentration. Incorporating photothermal nanoparticles into the coating markedly raised the surface temperature, and at a greater nanoparticle content, surface temperatures were also warmer, demonstrating improved photothermal conversion because of the light absorption properties of Fe_3O_4 nanoparticles. However, the temperature increase was not consistent across all nanoparticle types. For SiFPU, the ΔT values for the 5 % and 10 % nanoparticle concentrations were nearly identical, indicating that increasing the concentration beyond a certain level does not significantly enhance the photothermal effect. After the initial rapid rise in temperature within the first 10 min of irradiation, the rate of temperature increases slowed and plateaued (Fig. 10b–d), likely because of heat loss balancing heat input—indicating that the photothermal response reached a thermal equilibrium with the surrounding environment. This behavior highlights the importance of optimizing nanoparticle concentrations for effective photothermal performance, with diminishing returns at higher concentrations. Additionally, the initial heating rate (dT/dt), calculated as the slope of temperature rise during the first 60 s of irradiation, was determined to be 9.01 °C/min for 10FPU, 10.37 °C/min for 10SiFPU, and 9.28 °C/min for 10FOHPU coatings. These values quantitatively demonstrate that SiFPU coatings achieve the fastest early-stage photothermal heating, consistent with their lower bandgap.

Fig. 11 presents the photothermal performance of polyurethane (PU) coatings under two light intensities: 1 sun and 1.5 sun. Bare aluminum (Al) exhibited a minimal temperature increase (0.6 °C at 1 sun and 0.7 °C at 1.5 sun), reflecting its low photothermal efficacy. In contrast, PU coatings exhibited temperature increases with ΔT values of 10 and 13 °C under 1 sun and 1.5 sun, respectively. Adding Fe_3O_4 nanoparticles further enhanced the photothermal response, with 10FPU coatings showing ΔT values of 27.7 and 34 °C, at 1 and 1.5 sun, respectively. The 10SiFPU coating outperformed all other samples (ΔT values of 31.9 and 44.5 °C at 1 and 1.5 sun, respectively). This improvement results from the silicone oil coating, which promotes nanoparticle migration to the surface and reduces the band gap, thereby optimizing the light absorption. Similarly, the 10FOHPU coatings showed considerable photothermal enhancement, with ΔT values of 28.9 and 37.1 °C. These results emphasize the importance of nanoparticle concentration, surface modifications, and light intensity in enhancing the photothermal performance of the coatings.

3.5. Anti-icing properties

3.5.1. Quasi-liquid layer (QLL) characterization

ATR-FTIR spectroscopy was used as a reliable and effective technique to verify the presence of a quasi-liquid layer (QLL) and study its behavior. The evanescent wave of the reflected IR beam was used as a sensitive tool to probe functional groups located near the interface between the ATR crystal and the sample [49]. This approach is particularly

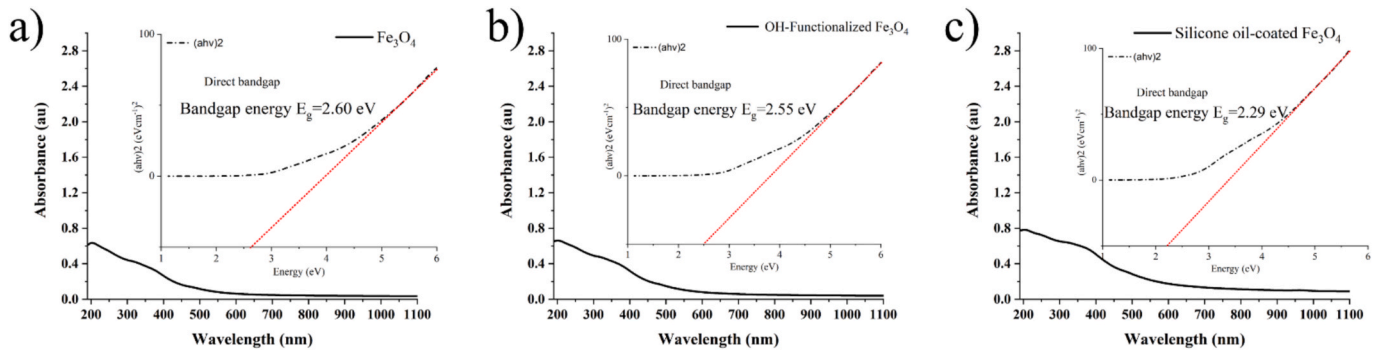

Fig. 9. Absorption spectra of the (a) Fe_3O_4; (b) Fe_3O_4-OH; and (c) silicone oil–coated Fe_3O_4 nanoparticles.

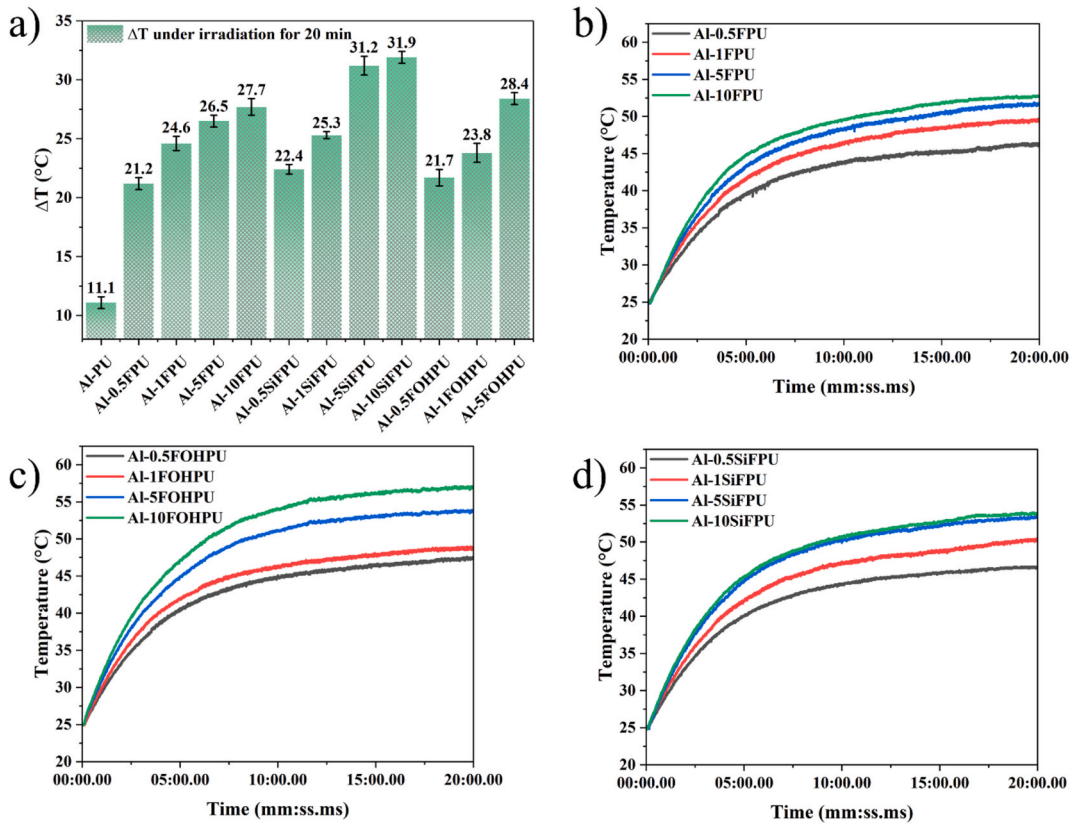

Fig. 10. Photothermal properties of the PU coatings with varying nanoparticle concentrations and compositions; (a) surface temperature increase (ΔT) after 20 min of irradiation for PU coatings differing in their concentrations of FPU, FOHPU, and SiFPU; temperature over time for the (b) FPU, (c) FOHPU, and (d) SiFPU coatings.

suited for analyzing temperature-dependent changes in the OH or OD stretching absorbance bands of H_2O or D_2O, which shift to a lower frequency. The FTIR spectra of D_2O before and after freezing demonstrate a shift of the O–D stretching band from 2467 to 2331 cm^{-1} at −8 °C during freezing (Fig. 12).

ATR-FTIR spectra of the polyurethane (PU) and 10FOHPU coatings, each in contact with heavy water (D_2O), were collected across a range of temperatures as the samples cooled (Fig. 13). The 10FOHPU/D_2O coating shows a characteristic peak at 2464 cm^{-1} at temperatures above 0 °C (Fig. 13a). This peak corresponds to the O–D stretching vibration in liquid D_2O, and its position is similar to that observed for bulk D_2O. A slight difference in the peak position is likely caused by interactions between D_2O and the 10FOHPU coating. As the temperature decreased to −20 °C, no shift of the band to 2451 cm^{-1}, typically associated with solid D_2O (ice), was observed. In contrast, the O–D stretching band of the unmodified PU coating shifted in position because of the D_2O phase transition from liquid to solid between 0 and −20 °C (Fig. 13b). This spectral change suggests that the D_2O absorbed on the surface of the PU coating froze at approximately −14 to −15 °C [36]. The difference in freezing temperatures, as indicated by the O–D stretching band shift, between the unmodified PU and 10FOHPU, likely results from a more substantial QLL on the modified coating. The thicker QLL on the 10FOHPU surface, along with its interactions with the coating material, hindered ice formation, as nucleation and growth of ice crystals at the interface were impeded by the QLL, preventing the arrangement of water molecules into the highly ordered crystalline structure characteristic of ice.

3.5.2. *Ice adhesion*

Push-off tests were performed to evaluate the ice adhesion strength of the three types of coatings (Fig. 14a). Ice adhesion strength varied significantly depending on the nanoparticle type and concentration in

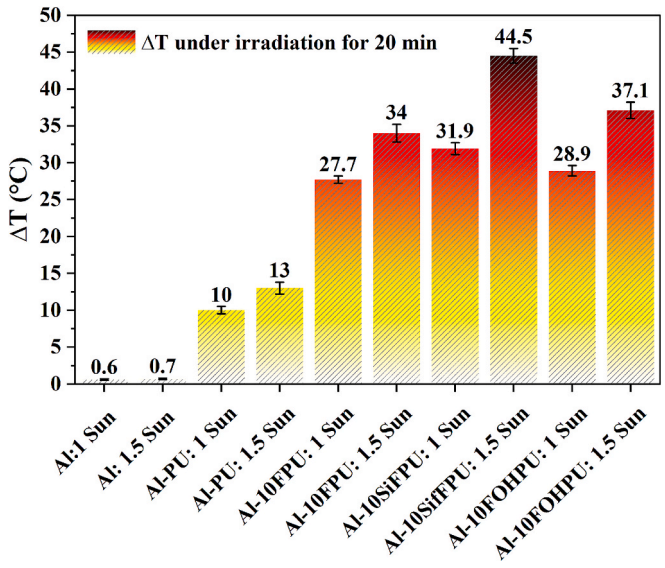

Fig. 11. Photothermal performance of the various coatings differing in their nanoparticle concentrations and compositions under 1 sun and 1.5 sun irradiation.

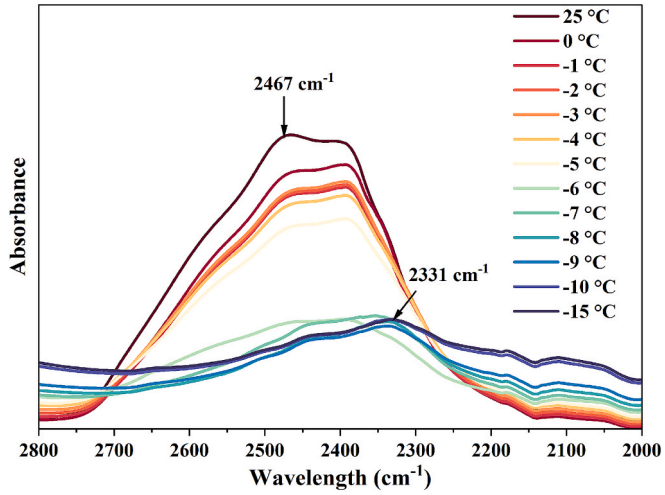

Fig. 12. ATR-FTIR spectra of D_2O throughout the cooling process.

the polyurethane coating. For the FPU coatings, higher nanoparticle concentrations increased the ice adhesion strength, peaking for 10FPU (290 ± 20 kPa) because of the greater surface roughness that enhances mechanical bonding with ice. However, this roughness did not significantly improve the wetting behavior, which is essential for anti-icing applications. Therefore, although higher concentrations of FPU nanoparticles increase ice adhesion, they do not necessarily enhance the de-icing or anti-icing performance. In contrast, SiFPU coatings showed a decrease in ice adhesion with an increase in the nanoparticle percentage. For 10SiFPU, the strength dropped to 75 ± 14 kPa, which is much lower than that of the FPU coatings. The silicone oil coating lowers surface tension, weakening the bond between the ice and the surface, which improves anti-icing properties. The reduced surface energy of silicone oil facilitates easier separation of ice from the surface. For FOHPU coatings, the hydroxyl groups on the nanoparticles create a QLL at the interface, reducing ice adhesion as described in our previous work [50]. These hydroxyl groups strongly interact with nearby water molecules through hydrogen bonding, leading to the formation of a disordered interfacial structure that is known as a quasi-liquid layer (QLL). This hydrated interfacial layer prevents ice from forming strong bonds with the solid surface, thereby lowering the mechanical interlocking and adhesion forces at the ice/surface interface. As the concentration of hydroxyl-functionalized nanoparticles increased, ice adhesion strength decreased, reaching a minimum at 10FOHPU (115 ± 12 kPa). Therefore, QLL formation greatly enhances the coating's resistance to ice adhesion, making it effective for anti-icing applications. However, for practical industrial applications, coatings must retain their icephobic properties even after numerous icing/de-icing cycles, not just exhibit low initial ice adhesion. To evaluate long-term durability, icephobicity was evaluated over 14 repeated icing and de-icing cycles using push-off adhesion measurements. The results depicted in Fig. 14b demonstrate that while SiF and FOH nanoparticles initially contribute to a decrease in ice adhesion strength for the polyurethane coatings, this effect diminishes after several icing-deicing cycles, although both remain lower than PU and FPU. This indicates that the SiFPU and FOHPU coatings retain their anti-icing efficacy even after multiple cycles, due to their low surface energy and QLL formation, respectively, which continue to reduce ice adhesion strength over time. In the case of 10FPU, the adhesion strength increased from 290 ± 20 kPa to 536 ± 15 kPa over the cycles, indicating that mechanical interlocking becomes stronger with repeated icing-deicing cycles, making it less suitable for durable anti-icing applications.

3.5.3. *Photothermal de-icing properties*

The coatings' de-icing performance is shown in Fig. 15b, which depicts the time required for ice to melt completely under controlled light conditions. A clear trend was observed: increasing the concentration of Fe_3O_4 nanoparticles significantly reduced the de-icing time. For the FPU coatings, the de-icing time for the 0.5FPU coating was 350 s, which dropped to 140 s for the 10FPU coating (Fig. 15a). This suggests that higher nanoparticle concentrations facilitate faster de-icing through an enhanced photothermal conversion. Similarly, the SiFPU coatings showed reduced de-icing times, with 0.5SiFPU starting at 540 s and 10SiFPU reaching 125 s. This improvement is likely because of the silicone oil's surface tension–reducing properties, which enhance nanoparticle dispersion and improve heat transfer, thereby reducing ice adhesion. For the FOHPU coatings, the 10FOHPU coating achieved the fastest de-icing time of 109 s, significantly faster than the 0.5FOHPU coating, which required 343 s. This enhanced performance in FOHPU coatings results from hydroxyl-functionalized nanoparticles that promote a QLL, reducing ice adhesion and accelerating de-icing. It is worth noting that the unmodified PU coating was unable to melt the ice droplet even after 2 h of light irradiation.

3.5.4. *Anti-icing properties under simulated sunlight*

Ice adhesion tests were performed before and after 20 min of simulated sun exposure to assess the anti-icing efficacy of polyurethane (PU) and modified PU coatings (Fig. 16). The ice adhesion strength of the pure PU coating was initially 271 ± 16 kPa and decreased to 230 ± 9 kPa after illumination. 10FPU, containing unmodified Fe_3O_4, exhibited greater ice adhesion (290 ± 20 kPa) than pure PU; this can be attributed to the increased surface roughness from the Fe_3O_4 nanoparticles, which enhances mechanical interlocking between the ice and the coating surface. However, after 20 min of solar exposure, the 10FPU ice adhesion decreased to 150 ± 11 kPa, likely because of the photothermal effect of the Fe_3O_4 nanoparticles converting simulated sunlight into heat and weakening the ice–surface interface.

Both the 10SiFPU (silicone oil–coated Fe_3O_4) and 10FOHPU (hydroxyl-functionalized Fe_3O_4) composites showed markedly lower ice adhesion strengths than pure PU, both before and after sun exposure. 10SiFPU had the lowest initial ice adhesion strength of 75 ± 14 kPa, which further decreased to 40 ± 8 kPa after exposure. This superior performance results from the low surface energy of the silicone oil coating. This low surface energy minimizes the ice–coating interactions and facilitates easier ice removal. The 10FOHPU coating had an initial value of 115 ± 12 kPa and decreased to 55 ± 10 kPa after exposure. Its enhanced icephobicity is attributed to the hydroxyl groups on the

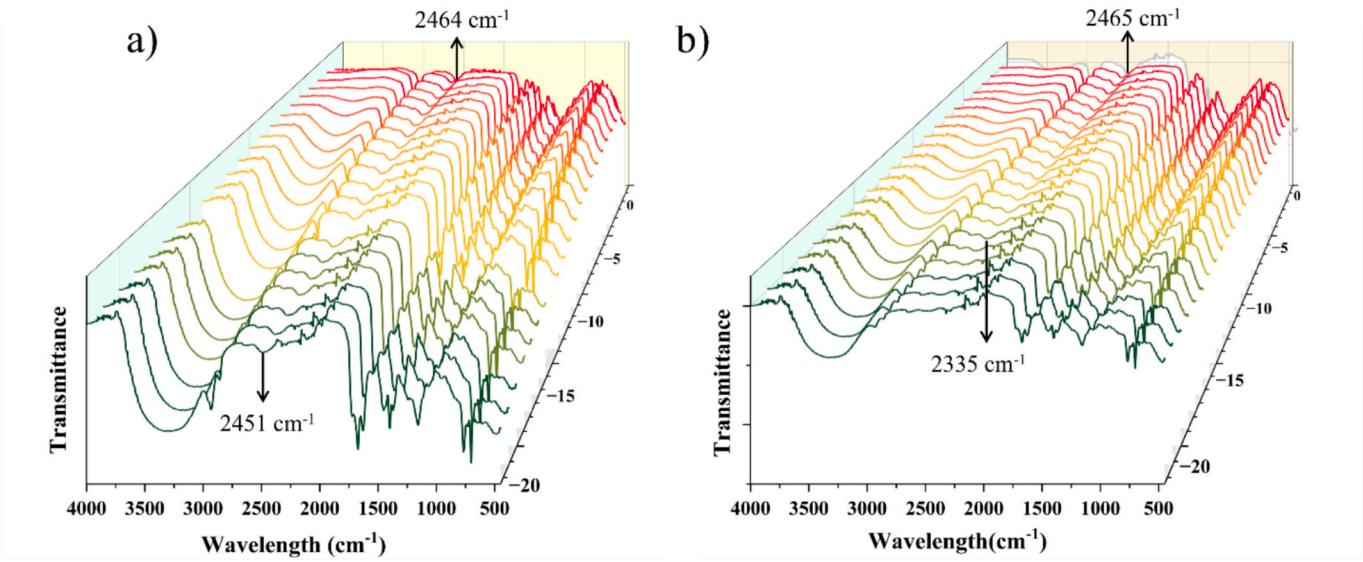

Fig. 13. ATR-FTIR spectra of the a) 10FOHPU/D_2O and b) PU/D_2O coatings during the cooling process.

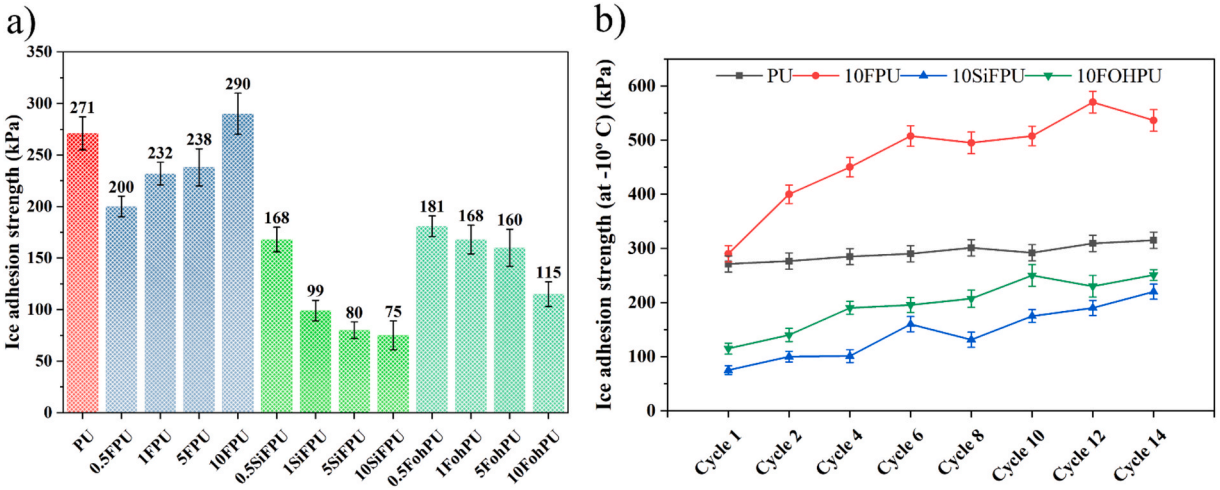

Fig. 14. (a) Ice adhesion strength of the polyurethane (PU) coatings containing differing concentrations of Fe_3O_4 (FPU), hydroxyl-functionalized Fe_3O_4 (SiFPU), and silicone oil–coated Fe_3O_4 (FOHPU) nanoparticles; (b) ice adhesion strength (kPa) of PU, 10FPU, 10FOHPU, and 10SiFPU coatings over 14 icing/de-icing cycles, evaluated using push-off tests to assess durability.

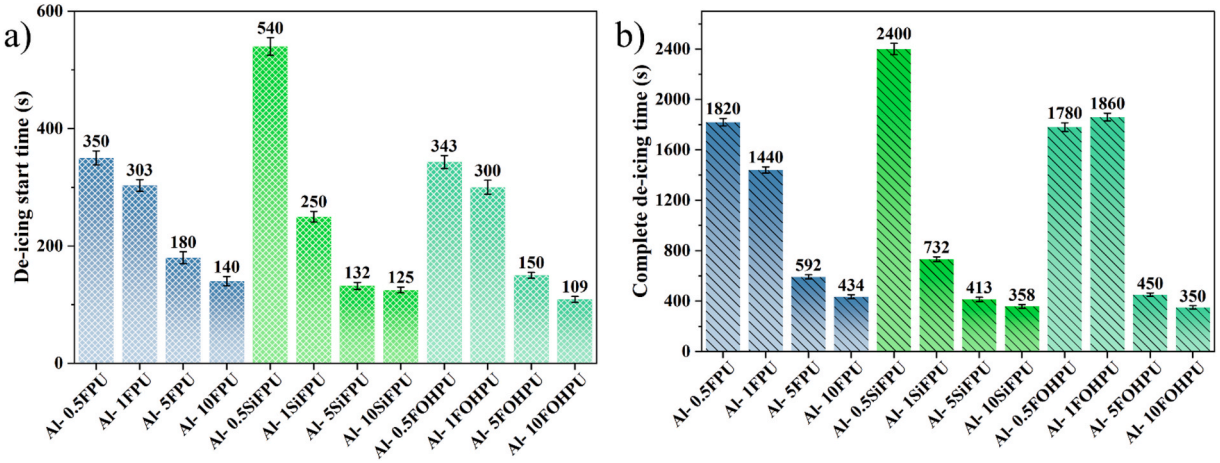

Fig. 15. De-icing performance of different coatings under light irradiation; a) de-icing start times and b) de-icing completion times for coatings containing differing concentrations of Fe_3O_4 (FPU), hydroxyl-functionalized Fe_3O_4 (SiFPU), and silicone oil–coated Fe_3O_4 (FOHPU) nanoparticles.

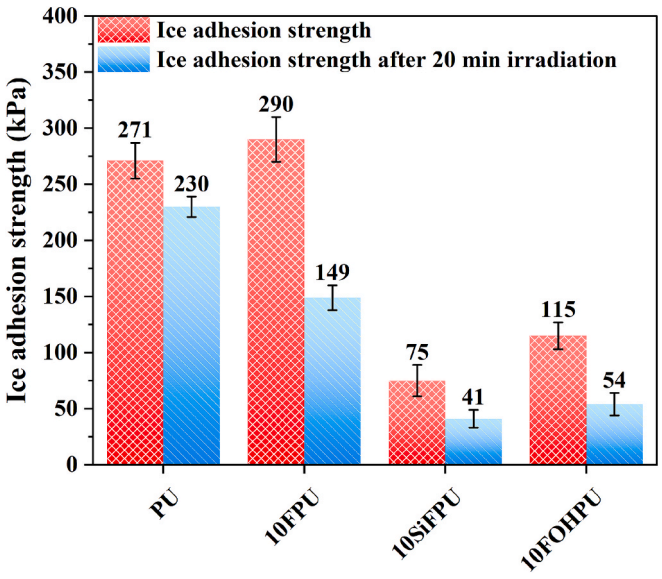

Fig. 16. Ice adhesion strength of the PU, 10FPU, 10SiFPU, and 10FOHPU coatings before and after exposure to simulated sunlight (1 sun (.

nanoparticle surface, which promote the formation of a QLL at the ice–coating interface. The QLL acts as a lubricant to greatly reduce the force required to detach the ice. The further reduction in ice adhesion after solar exposure for all modified samples illustrates the combined benefits of inherent icephobicity (from surface chemistry and/or roughness) and photothermal conversion. Thus, these coatings, particularly 10SiFPU and 10FOHPU, may be effective in both passive and active anti-icing applications.

4. Conclusions

Incorporating iron oxide (Fe_3O_4) nanoparticles with varying functionalization into polyurethane (PU) coatings significantly enhanced their photothermal and anti/de-icing performance. Specifically, silicone oil–coated (SiFPU) and hydroxyl-functionalized (FOHPU) Fe_3O_4 nanoparticles outperformed both pure PU and bare Fe_3O_4 (FPU) in multiple key areas. This superior performance stems from the tailored surface chemistry of the nanoparticles. The silicone oil coating on SiFPU reduced the surface energy to produce the lowest ice adhesion values (40 ± 8 kPa after simulated sun exposure) and rapid de-icing initiation (125 s at 10 % concentration). Hydroxyl functionalization in FOHPU created a stable QLL (confirmed by ATR-FTIR), even at −20 °C, producing remarkably low ice adhesion and rapid de-icing (109 s at 10 % concentration). While 10SiFPU initiates de-icing slightly faster than 10FOHPU, it results in an approximate 38 % decrease in tensile strength. In contrast, 10FOHPU maintains and even enhances mechanical performance while providing similarly quick de-icing. UV–Vis spectroscopy confirmed that both the coating and functionalization improved the light absorption properties of the Fe_3O_4 nanoparticles. Increasing nanoparticle concentrations, particularly up to 10 %, consistently improved the surface roughness and photothermal conversion; this improvement led to more effective heat generation under simulated solar irradiation. Crucially, the combined effects of icephobicity (because of low surface energy or QLL formation) and photothermal heating from the modified nanoparticles yielded a synergistic improvement in anti-icing performance. These findings provide a robust foundation for developing highly effective, multifunctional coatings for passive and active anti-icing/de-icing applications in various environments. Selecting nanoparticle functionalization strategically offers a powerful means of tailoring coating properties to meet specific performance demands. Our future research will concentrate on the enhancement of the anti-icing properties of the system by investigating additional strategies to mitigate ice adhesion. A promising approach is the creation of self-lubricating surfaces, which could complement the current photothermal and surface chemistry modifications to improve icephobic performance.

Declaration of Generative AI and AI-assisted technologies in the writing process

During the preparation of this work, the author(s) utilized large language models (LLMs), specifically GPT-4 by OpenAI and QuillBot, to enhance grammatical accuracy and improve the overall readability of the manuscript. Following the use of these tools, the author(s) reviewed and edited the content as needed and take(s) full responsibility for the content of the publication.

CRediT authorship contribution statement

Mohammad Bakhtiari: Writing – review & editing, Writing – original draft, Visualization, Validation, Software, Methodology, Investigation, Formal analysis, Data curation, Conceptualization. **Gelareh Momen:** Writing – review & editing, Validation, Supervision, Resources, Project administration, Methodology, Funding acquisition, Conceptualization. **Reza Jafari:** Writing – review & editing, Validation, Supervision, Resources, Project administration, Methodology, Funding acquisition, Conceptualization.

Declaration of competing interest

The authors declare that they have no known competing financial interests or personal relationships that could have appeared to influence the work reported in this paper.

Acknowledgments

The authors gratefully acknowledge the financial support provided by the Natural Sciences and Engineering Research Council of Canada (NSERC).This research was supported by NSERC under grant ID DGECR-2020-00472.Additional support was provided by the Centre de Recherche sur les Systèmes Polymères et Composites à Haute Performance (CREPEC)and the Quebec Centre for Advanced Materials (QCAM). The authors also acknowledge the Chaire Institutionnelle de Recherche en Matériaux Antigivre Innovants (CiMAGI), Université du Québec à Chicoutimi (UQAC), and the Laboratoire International des Matériaux Antigivre (LIMA), for providing the necessary infrastructure to carry out this work.

References

[1] Z. Zhao, et al., Progress in mechanism design of functional composites for anti-ice/deicing materials, Surface Sci. Technol. 2 (1) (2024) 2.
[2] W. Shijin, Y. Yuande, C. Yanjun, Global snow-and ice-related disaster risk: a review, nat. Hazard. Rev. 23 (4) (2022) 03122002.
[3] A.R. Solangi, Icing Effects on Power Lines and Anti-Icing And De-Icing methods, UiT The Arctic University of Norway, 2018.
[4] Mustafa, A., A. Barabadi, and T. Markeset, *Risk assessment of wind farm development in ice proven area.* Mustafa, A.(2023). Risk and Resilience Assessment of Wind Farms Performance in Cold Climate Regions.(Doctoral thesis). https://hdl. handle. net/10037/28610., 2019.
[5] F.T. Lynch, A. Khodadoust, Effects of ice accretions on aircraft aerodynamics, Prog. Aerosp. Sci. 37 (8) (2001) 669–767.
[6] M. Manni, et al., The influence of icephobic nanomaterial coatings on solar cell panels at high latitudes, Sol. Energy 248 (2022) 76–87.
[7] H.K. Pazarlıoğlu, A.Ü. Tepe, K. Arslan, Thermohydraulic performance assessment of new alternative methods for anti-icing application against current application in an aircraft, Proc. Inst. Mech. Eng., Part E: J. Proc. Mech. Eng. 239 (3) (2025) 1477–1493.
[8] H.K. Pazarlıoğlu, A.Ü. Tepe, K. Arslan, Optimization of parameters affecting anti-icing performance on wing leading edge of aircraft, Avrupa Bilim Ve Teknoloji Dergisi 34 (2022) 19–27.

[9] S. Keshavarzi, et al., Temperature-dependent droplet impact dynamics of a water droplet on hydrophobic and superhydrophobic surfaces: an experimental and predictive machine learning–based study, Int. J. Heat Mass Transf. 195 (2022).
[10] S.G. Moghadam, et al., In-depth analysis of the effect of physicochemical properties of ionic liquids on anti-icing behavior of silicon based-coatings, Cold Reg. Sci. Technol. 216 (2023) 104007.
[11] O. Parent, A. Ilinca, Anti-icing and de-icing techniques for wind turbines: critical review, Cold Reg. Sci. Technol. 65 (1) (2011) 88–96.
[12] A. Nistal, B. Sierra-Martín, A. Fernández-Barbero, On the durability of icephobic coatings: a review, Materials 17 (1) (2024) 235.
[13] L. Zhou, R. Liu, X. Yi, Research and development of anti-icing/deicing techniques for vessels: review, Ocean Eng. 260 (2022) 112008.
[14] J. Hu, G. Jiang, Superhydrophobic coatings on iodine doped substrate with photothermal deicing and passive anti-icing properties, Surf. Coat. Technol. 402 (2020) 126342.
[15] R. Rekuviene, et al., A review on passive and active anti-icing and de-icing technologies, Appl. Therm. Eng. 250 (2024) 123474.
[16] A. Khadak, B. Subeshan, R. Asmatulu, Studies on de-icing and anti-icing of carbon fiber-reinforced composites for aircraft surfaces using commercial multifunctional permanent superhydrophobic coatings, J. Mater. Sci. 56 (2021) 3078–3094.
[17] S. Peng, et al., Superhydrophobic coating with electro-photo-thermal conversion properties for all-weather anti-icing, Sol. Energy 270 (2024) 112384.
[18] Q. Li, et al., A review of efficient thermal application for ice detection and anti/de-icing technology, Appl. Therm. Eng. 263 (2025) 125366.
[19] S. Li, et al., A photothermal superhydrophobic coating with un-fluorinated modified CNTs for anti-icing applications on concrete, Mater. Lett. 355 (2024) 135463.
[20] H. Zhang, et al., Photothermal anti/de-icing performances of superhydrophobic surfaces with various micropatterns, Trans. Nanjing Univ. Aeronaut. Astronaut. 40 (2) (2023) 137–147.
[21] Z. Xie, et al., Recent progress in anti-icing and deicing applications of the photothermal conversion materials, Prog. Org. Coat. 184 (2023) 107834.
[22] S. Dash, J. de Ruiter, K.K. Varanasi, Photothermal trap utilizing solar illumination for ice mitigation, Sci. Adv. 4 (8) (2018) eaat0127.
[23] P. Cheng, D. Wang, P. Schaaf, A review on photothermal conversion of solar energy with nanomaterials and nanostructures: from fundamentals to applications, Adv. Sustainable Syst. (2022).
[24] G. Baffou, et al., Photoinduced heating of nanoparticle arrays, ACS Nano 7 (8) (2013) 6478–6488.
[25] Z. He, et al., Electro-/photo-thermal promoted anti-icing materials: a new strategy combined with passive anti-icing and active de-icing, Adv. Mater. Interfaces 9 (16) (2022) 2200275.
[26] E. Ye, Z. Li, Photothermal nanomaterials, Royal Society of Chemistry, 2022, p. 54.
[27] Y. Lei, et al., Ice-resistant Fe3O4@ PPy coating: Enhancing stability and durability with photothermal super hydrophobicity, Prog. Org. Coat. 196 (2024) 108704.
[28] X. Yin, et al., Integration of self-lubrication and near-infrared photothermogenesis for excellent anti-icing/deicing performance, Adv. Funct. Mater. 25 (27) (2015) 4237–4245.
[29] T. Cheng, et al., Magnetic particle-based super-hydrophobic coatings with excellent anti-icing and thermoresponsive deicing performance, J. Mater. Chem. A 3 (43) (2015) 21637–21646.
[30] E. Mitridis, et al., Metasurfaces leveraging solar energy for icephobicity, ACS Nano 12 (7) (2018) 7009–7017.
[31] G. Jiang, et al., Superhydrophobic SiC/CNTs coatings with photothermal deicing and passive anti-icing properties, ACS Appl. Mater. Interfaces 10 (42) (2018) 36505–36511.
[32] C. Wu, et al., Highly efficient solar anti-icing/deicing via a hierarchical structured surface, Mater. Horiz. 7 (8) (2020) 2097–2104.
[33] W. Ma, et al., Solar-assisted icephobicity down to −60°C with superhydrophobic selective surfaces, Cell Rep. Phys. Sci. 2 (3) (2021).
[34] S. Wu, et al., Superhydrophobic photothermal icephobic surfaces based on candle soot, Proc. Natl. Acad. Sci. 117 (21) (2020) 11240–11246.
[35] X. Yang, et al., Ultra-durable photothermal anti-/de-icing superhydrophobic coating with water droplets freezing from the outside in, J. Colloid Interface Sci. 682 (2025) 1127–1139.
[36] M.S. Koochaki, et al., Enhancing icephobic coatings: exploring the potential of dopamine-modified epoxy resin inspired by mussel catechol groups, Biomimetics 9 (6) (2024) 349.
[37] V. Shukla, Role of spin disorder in magnetic and EMI shielding properties of Fe3O4/C/PPy core/shell composites, J. Mater. Sci. 55 (7) (2020) 2826–2835.
[38] S. Singh, N. Goswami, Structural, optical, magnetic and dielectric properties of magnetite (Fe3O4) nanoparticles prepared by exploding wire technique, J. Mater. Sci. Mater. Electron. 32 (22) (2021) 26857–26870.
[39] Y.L. Chen, et al., SiO 2 passivation layer grown by liquid phase deposition for N-type bifacial silicon solar, Cells (2016).
[40] C.J. Huang, J.-R. Chen, S.P. Huang, Silicon dioxide passivation of gallium arsenide by liquid phase deposition, Mater. Chem. Phys. 70 (1) (2001) 78–83.
[41] W. Duan, et al., Synthesis and microwave absorption properties of SiC nanowires reinforced SiOC ceramic, J. Eur. Ceram. Soc. 34 (2) (2014) 257–266.
[42] S. Liu, et al., Preparation, surface functionalization and application of Fe3O4 magnetic nanoparticles, Adv. Colloid Interface Sci. 281 (2020) 102165.
[43] M.D. Nguyen, et al., Fe3O4 nanoparticles: structures, synthesis, magnetic properties, surface functionalization, and emerging applications, Appl. Sci. 11 (23) (2021) 11301.
[44] S. Goharshenas Moghadam, et al., To be or not to be a hydrophobic matrix? the role of coating hydrophobicity on anti-icing behavior and ions mobility of ionic liquids, Chem. Eng. J. 485 (2024) 149696.
[45] E. Bakhshandeh, et al., From theory to application: innovative ice-phobic polyurethane coatings by studying material parameters, mechanical insights, and additives, Surf. Interfaces 51 (2024) 104545.
[46] E. Hasa, Nano/Microstructured Materials Obtained Using Photopolymerization Induced Phase Separation, The University of Iowa, 2020.
[47] E. Bakhshandeh, et al., New insights into tailoring physicochemical properties for optimizing the anti-icing behavior of polyurethane coatings, J. Appl. Polym. Sci. 140 (44) (2023) e54610.
[48] Y. Zhao, et al., Photothermal effect on Fe3O4 nanoparticles irradiated by white-light for energy-efficient window applications, Sol. Energy Mater. Sol. Cells 161 (2017) 247–254.
[49] D. Chen, et al., Icephobic surfaces induced by interfacial nonfrozen water, ACS Appl. Mater. Interfaces 9 (4) (2017) 4202–4214.
[50] M. Bakhtiari, et al., Enhancing anti-icing efficacy in hybrid polyurethane coatings: evaluating the significance of molecular weight, chemical structure, and content of PEG/PDMS, Appl. Surf. Sci. 684 (2025) 161951.